Analysis of polarization effects on nanoscopic objects in the near-field optics

N. Richard
Abteilung Experimentelle Physik, Albert-Einstein Allee 11, D-89069 Universität Ulm, Germany
(Received 15 February 2000; published 12 January 2001)

This paper deals with the analysis of polarization around nanoscopic objects in near-field optics. The objects are illuminated through a transparent glass substrate under the condition of total internal reflection. The use of dielectric and metallic materials in the optical images is discussed. Using numerical simulations based on the Green's dyadic technique, we compute the total transmitted intensity of the scattered light and the different Cartesian components associated with the electric field in the attenuated total reflection configuration at constant height. The role of localized plasmon resonance is brought to the fore in the optical images of nanoscopic metallic objects. This paper shows that it is possible to reduce the interferences due to backward scattering from nanoscopic objects thanks to this polarimetry analysis. [S1063-651X(00)11309-1]

DOI: 10.1103/PhysRevE.63.026602 PACS number(s): 42.25.Fx, 42.25.Ja, 42.68.Mj, 78.66.−w

I. INTRODUCTION

Optical microscopes [photon scanning tunneling microscope (PSTM) and scanning near-field optical microscope (SNOM)] are based on the detection of the intensity associated with the total electric field [1–5]. In particular, these microscopes are presently considered as tools for the detection of optical signals associated with the total electric field $|\vec{E}|^2$, using a dielectric tip in transmission for illumination in total internal reflection (PSTM configuration) or the detection in far-field by illuminating objects by a tip (SNOM configuration). In order to study locally the polarimetry in near-field optics for the PSTM configuration, it is necessary to use tips which can detect one of the Cartesian components associated with the electric field. Unfortunately, up to now, these kinds of tips have not existed. However, the functionality allowing one to detect a signal proportional to the total optical magnetic field intensity $|\vec{H}|^2$ associated with the light-wave was brought to the fore recently by using metallized tips [6,7]. The components which were not in the incident electric field were created by the tridimensional structure in the near-field optics. A polarization analyzer at the exit of the fiber tip allows one to detect one of the Cartesian components. The signal detected when turning the output analyzer is thus related to one of the components relative to the electric field scattered by the three-dimensional objects deposited on a transparent substrate in the near-field optics. It is possible to detect at least one of the Cartesian components relative to the electric field scattered by tridimensional structures.

In magneto-optical thin films and three-dimensional array structures, polarization effects associated with the Kerr and Faraday effects in the far-field measurements [8,9] were considered. In this case, analysis of polarization shows the possibility of detecting a component of the electric field which was not in the incident field.

In this paper, we present numerical simulations to analyze the Cartesian components associated with the electric field scattered by nanoscopic objects in transmission. The objects are illuminated through a glass substrate under the condition of total internal reflection beyond the glass-air critical angle. Two modes of polarization are associated with the incoming light: TE and TM modes. We chose the incident light to be linearly polarized with the z direction being perpendicular to the glass-air interface. The TE mode (s polarization) corresponds to an incident electric field, pointing towards the x direction, perpendicular to the plane of incidence. The TM mode (p polarization) corresponds to a field parallel to the plane of incidence. The calculations are based on Green's dyadic technique using the Lippmann-Schwinger and Dyson equations for the computation of the scattered electric field and its associated Cartesian components.

Polarimetry studies are necessary to understand the scattered electric field behaviors in the near-field optical images analysis. In the PSTM configuration, surface waves appear due to the incident illumination. We will show that cutting the transmitted wave by analyzing at 90° from the incident electric field, it is possible to reduce the interferences due to the backscattering light scattered by the objects. These interferences alter the resolution of the near-field optical images. The surface waves due to scattering by mesoscopic objects are indeed predominant compared to the effects relative to the confinement of the total electric field close to the structures. These experimental studies will outline effects relative to the confinement of the electric field near the objects which are due to the topography of the defects deposited on the surface.

For this study, we will use different types of materials: dielectric and metallic objects deposited on a glass substrate. The role of localized plasmon resonance [10–12] will be considered for the case of noble metals. We will show that the absorption of different materials plays an important role in understanding optical near-field images. In Sec. II, we detail the numerical procedure based on Green's dyadic technique. Section III describes the near-field optical images for dielectric objects deposited on a glass substrate illuminated under the condition of total internal reflection. In Sec. IV, we report numerical simulations on metallic and nanometric objects with the same configuration of Sec. III. We chose to set a $100\times100\times40$ nm^3 object deposited on a glass substrate. The object is illuminated under the condition of total internal reflection with an angle of incidence $\theta=60°$.

The detection in the near-field optics is performed at constant height $e=100$ nm above the object. This height was

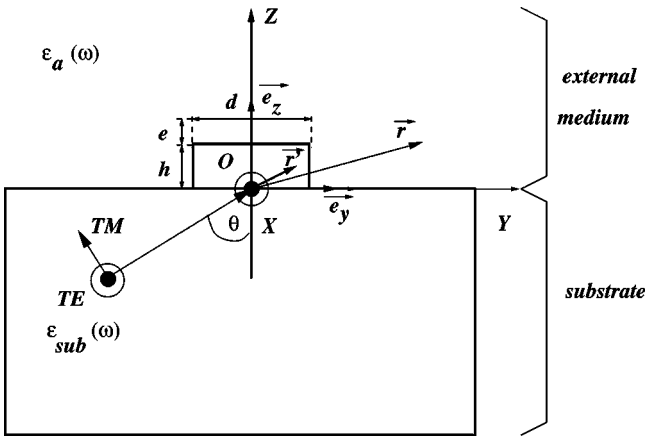

FIG. 1. Geometry of a surface system separating two dielectric media of permittivity $\varepsilon_a(\omega)=1$ ($z>0$, air) and $\varepsilon_{\text{sub}}(\omega)=2.25$ ($z<0$, glass substrate), configuration of total internal reflection, θ is the angle of incidence ($\theta=60°$), d is the lateral size of the pad ($d=100$ nm), h its height ($h=40$ nm), and e is the distance at which the detection is performed ($e=100$ nm). Two modes of polarization are associated with the incident beam: TE and TM modes.

chosen to show backscattering waves on the surface due to the defect. We consider that the index of refraction of the glass fixed to 1.5 does not depend on the incident wavelength. For the metallic objects, we took the optical constants compiled in Ref. [13].

II. SCATTERING THEORY FOR A SURFACE SYSTEM

Our theoretical analysis of the propagation of electromagnetic fields through arbitrary isotropic/anisotropic three-dimensional objects is based on scattering theory. In this theory, one describes the scattering of waves relative to a reference system. In the context of three-dimensional objects, it is convenient to use a system such as the single surface geometry composed of two semi-infinite isotropic media [14]. Let $\varepsilon_1(z,\omega)$ be the frequency (ω) dependent dielectric function profile of this surface system. Assuming that the electric and magnetic fields have a harmonic time dependence $e^{-i\omega t}$ in Maxwell's equations, the vectorial wave equation satisfied by the electric field is (c is the speed of light in vacuum)

$$-\vec{\nabla}\times\vec{\nabla}\times\vec{E}(\vec{r})+\frac{\omega^2}{c^2}\varepsilon_1(z,\omega)\vec{E}(\vec{r})=\overleftrightarrow{V}(z,\omega)\vec{E}(\vec{r}). \quad (1)$$

We introduce the surface (see Fig. 1) as follows.

For $z>0$, $\varepsilon_1(z,\omega)$ corresponds to the dielectric function of the external medium:

$$\varepsilon_1(z,\omega)=\varepsilon_a(\omega),$$

while for $z<0$, $\varepsilon_1(z,\omega)$ is given by the dielectric function of the substrate:

$$\varepsilon_1(z,\omega)=\varepsilon_{\text{sub}}(\omega).$$

The perturbation dyadic $\overleftrightarrow{V}(\vec{r},\omega)$ is defined by

$$\overleftrightarrow{V}(\vec{r},\omega)=\frac{\omega^2}{c^2}[\overleftrightarrow{1}\varepsilon_a(\omega)-\overleftrightarrow{\varepsilon}(\vec{r},\omega) \quad (z>0), \quad (2)$$

$$\overleftrightarrow{V}(\vec{r},\omega)=0 \quad (z<0). \quad (3)$$

$\overleftrightarrow{\varepsilon}(\vec{r},\omega)$ is the dielectric tensor of the three-dimensional objects which are located in the *upper* z plane ($z'>0$). The structure of this tensor is not limited to isotropic materials; the case of anisotropic materials can be treated because this technique can account for any kind of linear anisotropy.

The solution of the scattering problem is given by the Lippmann-Schwinger equation:

$$\vec{E}(\vec{r})=\vec{E}_0(\vec{r})+\vec{E}^s(\vec{r}), \quad (4)$$

where $\vec{E}_0(\vec{r})$ and $\vec{E}^s(\vec{r})$ are the incident and the scattered field.

We first show the two possible values of the wave-vector component along $\vec{e}_z$ ($k_\parallel^2=k_x^2+k_y^2$):

$$k_a=\sqrt{\frac{\omega^2}{c^2}\varepsilon_a-k_\parallel^2}, \quad (5)$$

$$k_{\text{sub}}=\sqrt{\frac{\omega^2}{c^2}\varepsilon_{\text{sub}}-k_\parallel^2}. \quad (6)$$

In the simple case where the incident field has the form of a plane wave, we have of course for $z'>0$ and $z>0$,

$$\vec{E}_0(\vec{r})=\vec{A}e^{i\vec{k}_t\cdot\vec{r}} \quad (z>0),$$

where we normalized the TE mode according to

$$\vec{A}=\frac{2k_{\text{sub}}}{k_{\text{sub}}+k_a}\vec{e}_x \quad (7)$$

and the TM mode as follows:

$$\vec{A}=\frac{2k_{\text{sub}}\sqrt{\varepsilon_a}\sqrt{\varepsilon_{\text{sub}}}}{k_{\text{sub}}\varepsilon_a+k_a\varepsilon_{\text{sub}}}(-\cos\theta_t\vec{e}_y+\sin\theta_t\vec{e}_z), \quad (8)$$

where θ_t is the angle of transmission, $\vec{k}_t=(\omega/c)\sqrt{\varepsilon_a}\times\sin\theta_t\vec{e}_y+(\omega/c)\sqrt{\varepsilon_a}\cos\theta_t\vec{e}_z=\vec{k}_\parallel+(\omega/c)\sqrt{\varepsilon_a}\cos\theta_t\vec{e}_z$, and $\vec{r}=(x,y,z)$.

The scattered field is given by [B is the domain where $\overleftrightarrow{V}(z',\omega)\neq 0$]

$$\vec{E}^s(\vec{r})=\int_B d\vec{r}'\,\overleftrightarrow{G}(\vec{r},\vec{r}';\omega)\overleftrightarrow{V}(z',\omega)\vec{E}(\vec{r}'). \quad (9)$$

In Eq. (9), $\overleftrightarrow{G}(\vec{r},\vec{r}';\omega)$ is Green's dyadic defined by [$\delta(\vec{r}-\vec{r}')$ is the Dirac delta function]

$$-\vec{\nabla}\times\vec{\nabla}\times\overleftrightarrow{G}(\vec{r},\vec{r}';\omega)+\frac{\omega^2}{c^2}\varepsilon_1(z,\omega)\overleftrightarrow{G}(\vec{r},\vec{r}';\omega)=\overleftrightarrow{1}\delta(\vec{r}-\vec{r}'). \quad (10)$$

The numerical analysis is based on the discretization of this last Lippmann-Schwinger equation [15].

This leads to the three-dimensional vector Lippmann-Schwinger equation:

$$\vec{E}(\vec{r}\,')=\vec{E}_0(\vec{r}\,')+\int_B d\vec{r}\,'\,\vec{\vec{G}}(\vec{r},\vec{r}\,';\omega)\vec{\vec{V}}(z',\omega)\vec{E}(\vec{r}\,'). \tag{11}$$

The numerical analysis is based on the discretization of this last Lippmann-Schwinger equation [15].

In order to solve the implicit equation (11), we discretize it in the direct space leading to a matrix equation:

$$\begin{pmatrix}\vec{E}_1\\ \vec{E}_2\\ \vdots\\ \vec{E}_N\end{pmatrix}=\begin{pmatrix}\vec{E}_1^0\\ \vec{E}_2^0\\ \vdots\\ \vec{E}_N^0\end{pmatrix}+\begin{pmatrix}w_1G_{11}V_1 & w_2G_{12}V_2 & \cdots & w_NG_{1N}V_N\\ w_1G_{21}V_1 & w_2G_{22}V_2 & \cdots & w_NG_{2N}V_N\\ \vdots & \vdots & \ddots & \vdots\\ w_1G_{N1}V_1 & w_2G_{N2}V_2 & \cdots & w_NG_{NN}V_N\end{pmatrix}\begin{pmatrix}\vec{E}_1\\ \vec{E}_2\\ \vdots\\ \vec{E}_N\end{pmatrix},$$

which can be expressed by

$$\underbrace{\left[\begin{pmatrix}1&0&\cdots&0\\0&1&\cdots&0\\ \vdots&\vdots&\ddots&\vdots\\0&0&\cdots&1\end{pmatrix}-\begin{pmatrix}w_1\,G_{11}\,V_1 & w_2\,G_{12}\,V_2 & \cdots & w_N\,G_{1N}\,V_N\\ w_1\,G_{21}\,V_1 & w_2\,G_{22}\,V_2 & \cdots & w_N\,G_{2N}\,V_N\\ \vdots & \vdots & \ddots & \vdots\\ w_1\,G_{N1}\,V_1 & w_2\,G_{N2}\,V_2 & \cdots & w_N\,G_{NN}\,V_N\end{pmatrix}\right]}_{M}\begin{pmatrix}\vec{E}_1\\ \vec{E}_2\\ \vdots\\ \vec{E}_N\end{pmatrix}=\begin{pmatrix}\vec{E}_1^0\\ \vec{E}_2^0\\ \vdots\\ \vec{E}_N^0\end{pmatrix}$$

N is the number of points used for the discretization and w_i, $i=1,N$ are the weights of the discretized integral (11).

In order to find the electric field inside and outside the multilayer structure, we just have to inverse the matrix M thanks to the LU factorization.

The source coordinate z' being positive, for $z>0$, the dyadic Green's tensor associated with the external medium $\vec{\vec{G}}_0(\vec{r},\vec{r}\,';\omega)$ and the surface response $\vec{\vec{G}}_s(\vec{r},\vec{r}\,';\omega)$ are added for the total response of the system:

$$\vec{\vec{G}}(\vec{r},\vec{r}\,';\omega)=\vec{\vec{G}}_0(\vec{r},\vec{r}\,';\omega)+\vec{\vec{G}}_s(\vec{r},\vec{r}\,';\omega).$$

Only the $z'>0$ and $z>0$ case will be considered in order to use the conventional approach in the photon scanning tunneling optical microscopy (PSTM) configuration [1,2].

Here, we detail the analytical structure of $\vec{\vec{G}}(\vec{r},\vec{r}\,';\omega)$. The homogeneous 3D Green's tensor is defined by

$$\vec{\vec{G}}_0(\vec{r},\vec{r}\,';\omega)=\frac{1}{4\pi^2}\int d\vec{k}_\parallel e^{i\vec{k}_\parallel\cdot(\vec{r}_\parallel-\vec{r}_\parallel')}\vec{\vec{g}}_0(z,z';\vec{k}_\parallel)+\frac{c^2}{\omega^2\varepsilon_a}\vec{\vec{L}}\,\delta(\vec{r}-\vec{r}\,'), \tag{12}$$

where the tensor $\vec{\vec{g}}_0(z,z';\vec{k}_\parallel)$ has the following form [16]:

$$\vec{\vec{g}}_0(z,z';\vec{k}_\parallel)=\frac{e^{ik_a|z-z'|}}{2ik_a}\left(\vec{\vec{1}}-\frac{c^2}{\omega^2\varepsilon_a}\vec{\vec{Q}}\right) \tag{13}$$

with

$$\vec{\vec{Q}}=\begin{pmatrix}k_x^2 & k_xk_y & \frac{|z-z'|}{z-z'}k_xk_a\\ k_xk_y & k_y^2 & \frac{|z-z'|}{z-z'}k_yk_a\\ \frac{|z-z'|}{z-z'}k_xk_a & \frac{|z-z'|}{z-z'}k_yk_a & k_a^2\end{pmatrix}. \tag{14}$$

In order to obtain $\vec{\vec{G}}_0(\vec{r},\vec{r}\,';\omega)$, we must integrate Eq. (12) on $\vec{k}_\parallel$. We know that

$$\frac{e^{ik_a|z-z'|}}{2ik_a}=\frac{1}{2\pi}\int dk_z\frac{e^{ik_z(z-z')}}{k_a^2-k_z^2}. \tag{15}$$

We thus obtain the following integral:

$$\vec{\vec{G}}_0(\vec{r},\vec{r}\,';\omega)=\int_{\vec{k}}d\vec{k}\left(\vec{\vec{1}}-\frac{1}{q^2}\vec{k}\otimes\vec{k}\right)\frac{e^{i\vec{k}(\vec{r}-\vec{r}\,')}}{8\pi^3(q^2-k^2)} \tag{16}$$

which can be written as follows:

$$\vec{\vec{G}}_0(\vec{r},\vec{r}\,';\omega)=-\left(\vec{\vec{1}}-\frac{1}{q^2}\vec{\nabla}\otimes\vec{\nabla}'\right)\frac{e^{iqR}}{4\pi R} \tag{17}$$

because

$$\int_{\vec{k}}d\vec{k}\frac{e^{i\vec{k}\cdot(\vec{r}-\vec{r}\,')}}{8\pi^3(q^2-k^2)}=-\frac{e^{iqR}}{4\pi R},$$

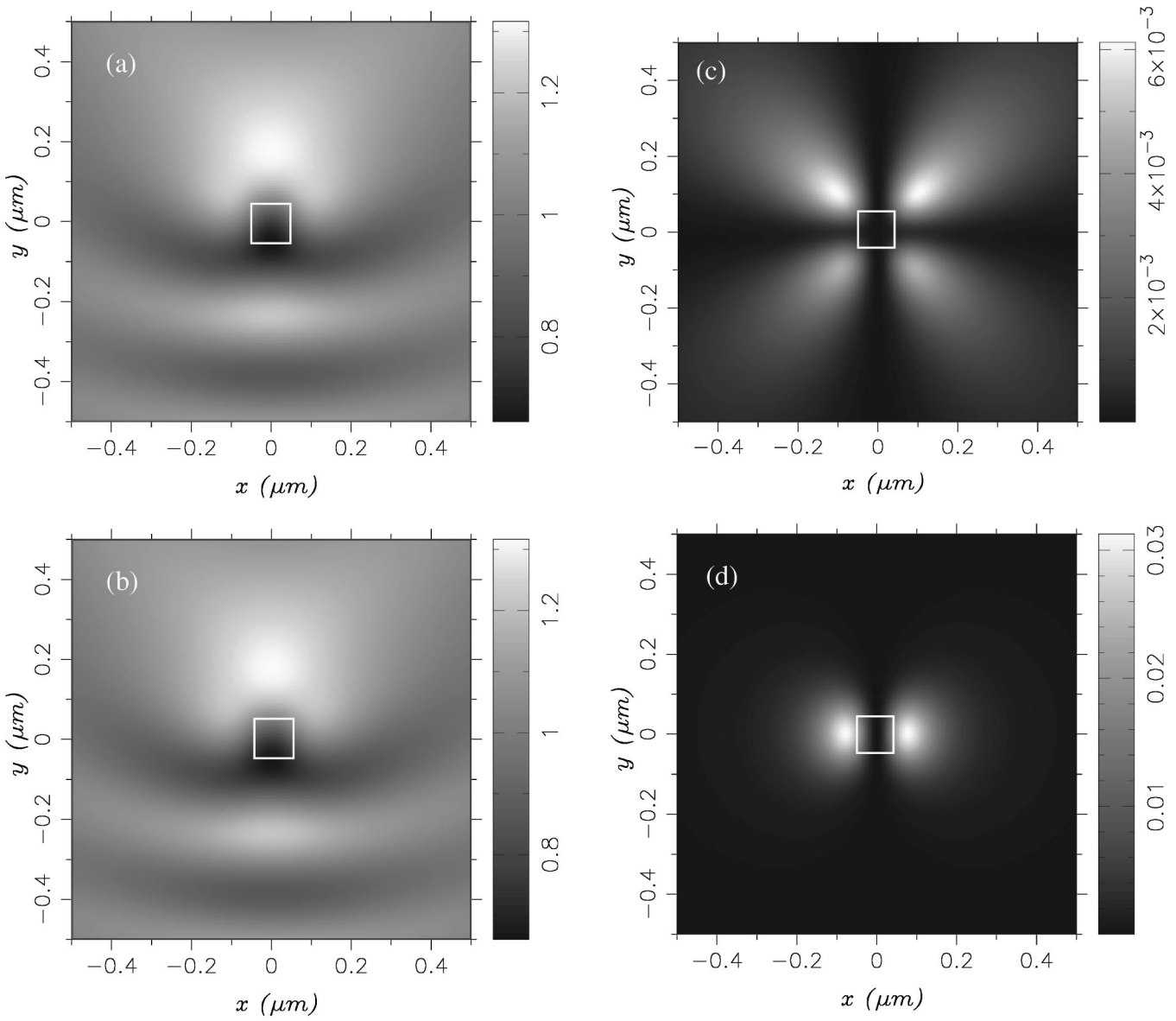

FIG. 2. A dielectric pad ($\varepsilon=10.0$) of $100\times100\times40$ nm^3 is deposited on a glass substrate. The incident beam is TE polarized with $\lambda=633$ nm. (a) Variation of the intensity associated with the total electric field. (b) Variation of the intensity associated with the x component of the electric field. (c) Variation of the intensity associated with the y component of the electric field. (d) Variation of the intensity associated with the z component of the electric field. The detection is performed at $e=100$ nm above the dielectric pad.

where $R=\|\vec{r}-\vec{r}'\|$. We start from Eq. (17), where we designate by $\vec{\nabla}'$ the gradient according to $\vec{r}'$. The calculation of this formula leads to

$$\vec{\vec{G}}_0(\vec{r},\vec{r}';\omega)=-\left(\vec{\vec{1}}-\vec{\vec{1}}\frac{1-iqR}{q^2R^2}-\vec{R}\otimes\vec{R}\frac{-3+3iqR+q^2R^2}{q^2R^4}\right)\frac{e^{iqR}}{4\pi R}.$$

The tensor

$$\vec{\vec{L}}=\begin{pmatrix}1/3 & 0 & 0\\ 0 & 1/3 & 0\\ 0 & 0 & 1/3\end{pmatrix} \tag{18}$$

accounts for the depolarization of a discretized cubic cell which has the shape of a sphere [17]. The dyadic $\vec{\vec{G}}_s(\vec{r},\vec{r}';\omega)$ describing the surface response when $z>0$ is

$$\vec{\vec{G}}_s(\vec{r},\vec{r}';\omega)=\frac{1}{4\pi^2}\int d\vec{k}_\parallel\, e^{i\vec{k}_\parallel\cdot(\vec{r}_\parallel-\vec{r}_\parallel')}\vec{\vec{g}}_s(z,z';\vec{k}_\parallel), \tag{19}$$

where the tensor $\vec{\vec{g}}_s(z,z';\vec{k}_\parallel)$ is written as

$$\vec{\vec{g}}_s(z,z';\vec{k}_\parallel)=\frac{1}{k_\parallel^2}\begin{pmatrix}k_x^2D_{xx}+k_y^2D_{yy} & k_xk_y(D_{xx}-D_{yy}) & k_\parallel k_xD_{xz}\\ k_xk_y(D_{xx}-D_{yy}) & k_y^2D_{xx}+k_x^2D_{yy} & k_\parallel k_yD_{xz}\\ k_\parallel k_xD_{zx} & k_\parallel k_yD_{zx} & k_\parallel^2D_{zz}\end{pmatrix}, \tag{20}$$

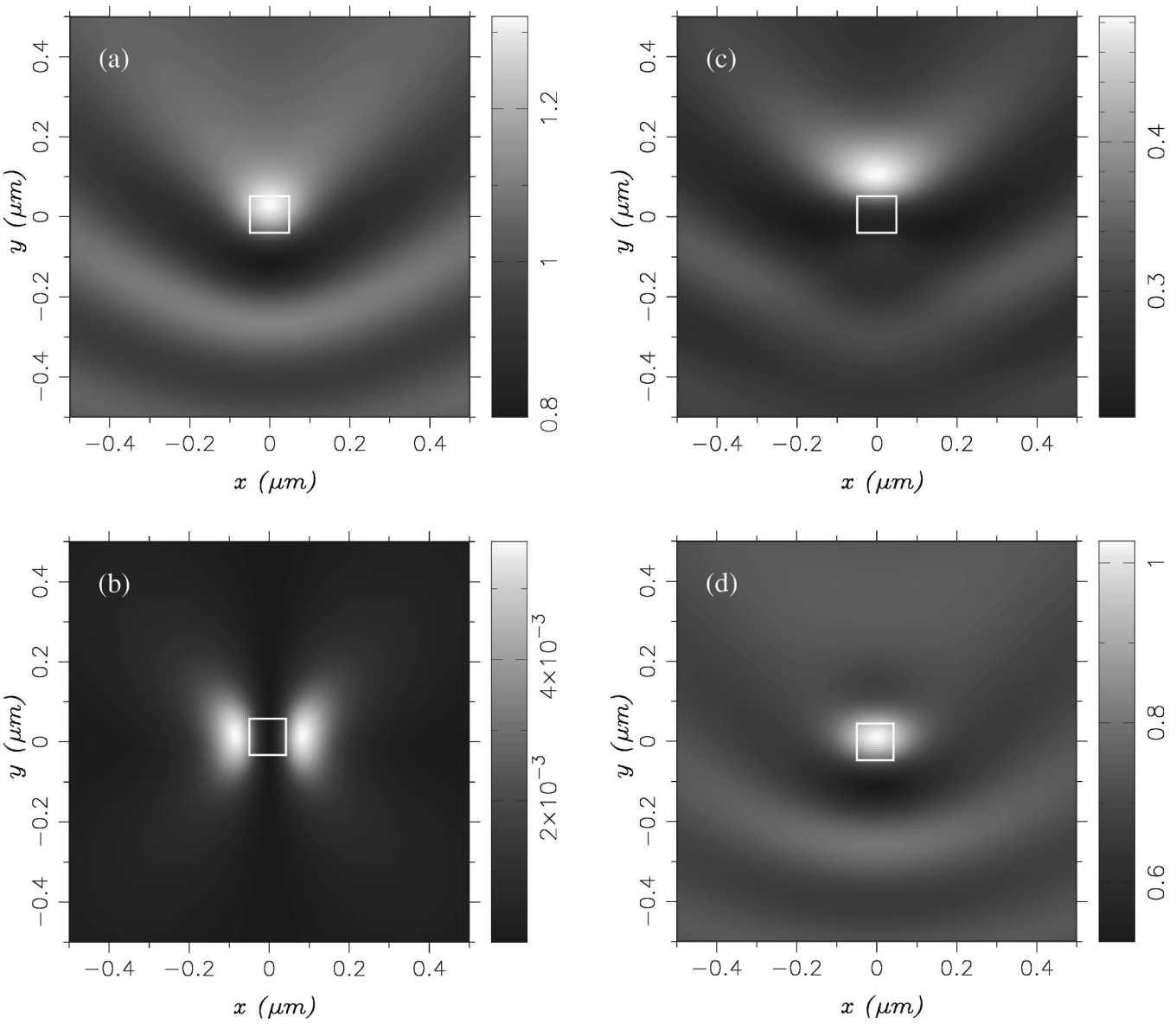

FIG. 3. A dielectric pad ($\varepsilon = 10.0$) of $100 \times 100 \times 40$ nm^3 is deposited on a glass substrate. The incident beam is TM polarized with $\lambda = 633$ nm. (a) Variation of the intensity associated with the total electric field. (b) Variation of the intensity associated with the x component of the electric field. (c) Variation of the intensity associated with the y component of the electric field. (d) Variation of the intensity associated with the z component of the electric field. The detection is performed at $e = 100$ nm above the dielectric pad.

where

$$D_{xx} = -\frac{c^2}{\omega^2 \varepsilon_a} k_a^2 \frac{k_a \varepsilon_{\text{sub}} - k_{\text{sub}} \varepsilon_a}{k_a \varepsilon_{\text{sub}} + k_{\text{sub}} \varepsilon_a} \frac{e^{ik_a(z+z')}}{2ik_a}, \tag{21}$$

$$D_{yy} = \frac{k_a - k_{\text{sub}}}{k_a + k_{\text{sub}}} \frac{e^{ik_a(z+z')}}{2ik_a}, \tag{22}$$

$$D_{zx} = \frac{c^2}{\omega^2 \varepsilon_a} k_a k_{\parallel} \frac{k_a \varepsilon_{\text{sub}} - k_{\text{sub}} \varepsilon_a}{k_a \varepsilon_{\text{sub}} + k_{\text{sub}} \varepsilon_a} \frac{e^{ik_a(z+z')}}{2ik_a}, \tag{23}$$

$$D_{xz} = -\frac{c^2}{\omega^2 \varepsilon_a} k_a k_{\parallel} \frac{k_a \varepsilon_{\text{sub}} - k_{\text{sub}} \varepsilon_a}{k_a \varepsilon_{\text{sub}} + k_{\text{sub}} \varepsilon_a} \frac{e^{ik_a(z+z')}}{2ik_a}, \tag{24}$$

$$D_{zz} = \frac{c^2}{\omega^2 \varepsilon_a} k_{\parallel}^2 \frac{k_a \varepsilon_{\text{sub}} - k_{\text{sub}} \varepsilon_a}{k_a \varepsilon_{\text{sub}} + k_{\text{sub}} \varepsilon_a} \frac{e^{ik_a(z+z')}}{2ik_a}. \tag{25}$$

We now write the surface Green's tensor 3D in the quasistatic approximation. The electrostatic approximation occurs when we neglect the delay effects related to the temporal evolution in the surface Green's tensor $\overleftrightarrow{G}_s(\vec{r},\vec{r};\omega)$. Therefore, we set the light speed tending towards infinity, as though the objects behave as electrostatic dipoles. It thus comes back to neglect the magnetic effects (we eliminate the magnetic field in Maxwell's equations by this approximation) and only the electric field scattered by the structure shows up. This approximation makes sense here because this study is based on small objects which are not so far away

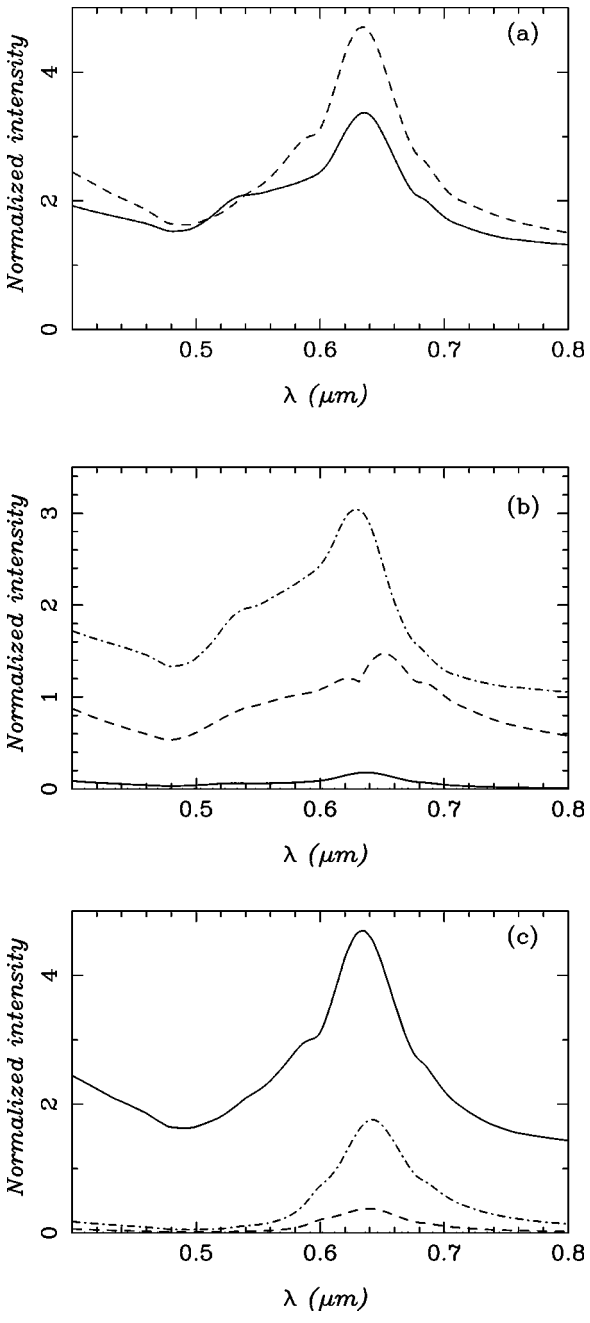

FIG. 4. A gold pad of $100\times100\times40$ nm^3 is deposited on a glass substrate. (a) Variation of the maximum intensity associated with the total electric field for the TM mode (solid line) and for the TE mode (dashed line) as a function of the incident wavelength. (b) Variation of the maximum intensity associated with the x component (solid line), the y component (dashed line), and the z component (dotted dashed line) of the electric field for the TM mode as a function of the incident wavelength. (c) Variation of the maximum intensity associated with the x component (solid line), the y component (dashed line), and the z component (dotted dashed line) of the electric field for the TE mode as a function of the incident wavelength. The detection is performed at $e=100$ nm above the metallic pad.

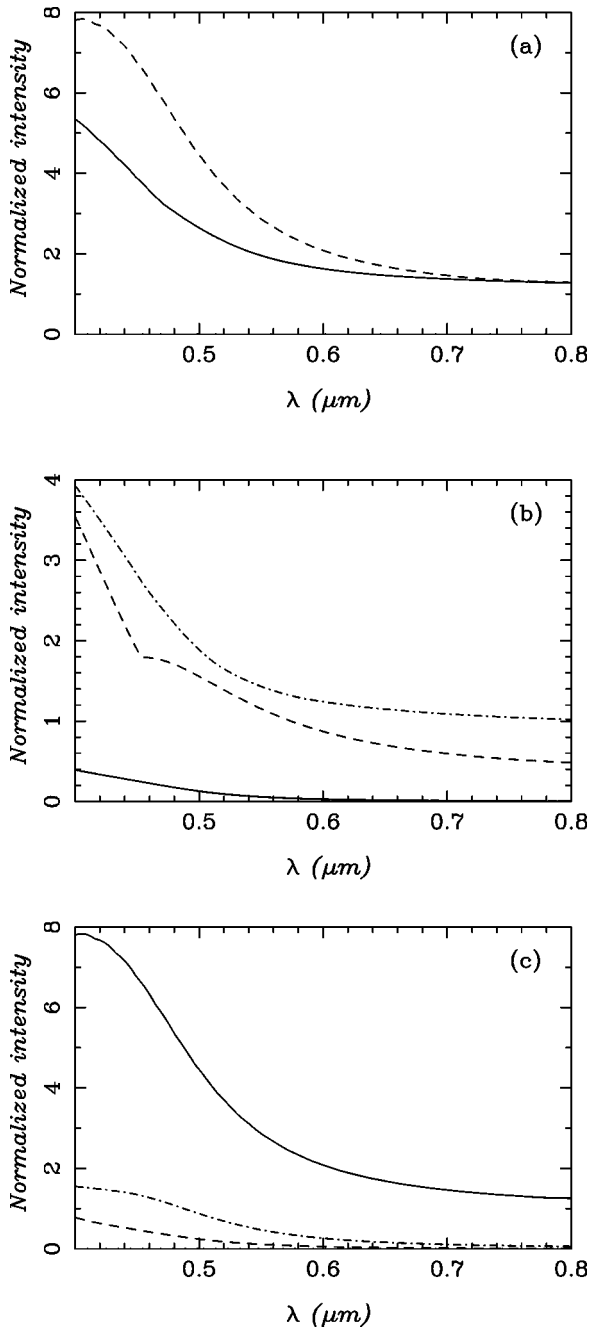

FIG. 5. An aluminum pad of $100\times100\times40$ nm^3 is deposited on a glass substrate. (a) Variation of the maximum intensity associated with the total electric field for the TM mode (solid line) and for the TE mode (dashed line) as a function of the incident wavelength. (b) Variation of the maximum intensity associated with the x component (solid line), the y component (dashed line), and the z component (dotted dashed line) of the electric field for the TM mode as a function of the incident wavelength. (c) Variation of the maximum intensity associated with the x component (solid line), the y component (dashed line), and the z component (dotted dashed line) of the electric field for the TE mode as a function of the incident wavelength. The detection is performed at $e=100$ nm above the metallic pad.

from each other. Moreover, the propagation and also the observation are realized for a distance close to the objects. Thus, the following calculations are only valid for small objects in the $z>0$ region and the observation will be done close to them in the medium of dielectric permittivity $\varepsilon_a(\omega)$. By integrating Eq. (19) on $\vec{k}_{\|}$, the Green's tensor elements relative to the surface (21)–(25) in the electrostatic approximation, we obtain

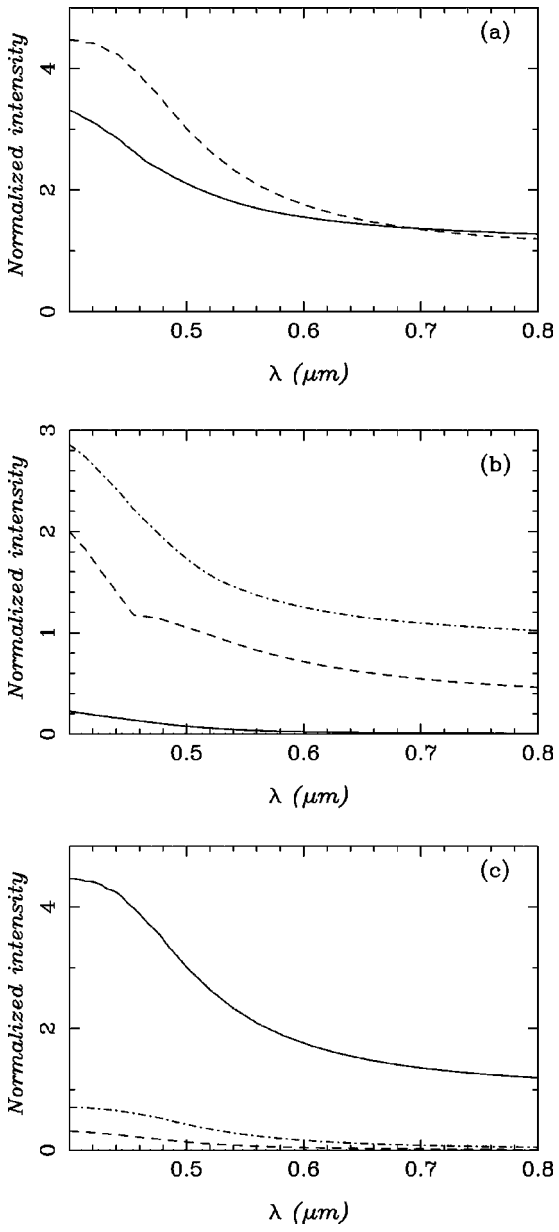

FIG. 6. A chromium pad of $100\times100\times40$ nm^3 is deposited on a glass substrate. (a) Variation of the maximum intensity associated with the total electric field for the TM mode (solid line) and for the TE mode (dashed line) as a function of the incident wavelength. (b) Variation of the maximum intensity associated with the x component (solid line), the y component (dashed line), and the z component (dotted dashed line) of the electric field for the TM mode as a function of the incident wavelength. (c) Variation of the maximum intensity associated with the x component (solid line), the y component (dashed line), and the z component (dotted dashed line) of the electric field for the TE mode as a function of the incident wavelength. The detection is performed at $e=100$ nm above the metallic pad.

$$\vec{\vec{G}}_s(\vec{r},\vec{r}';\omega)=\frac{1}{4\pi}\frac{c^2}{\omega^2\varepsilon_a}\frac{\varepsilon_{\text{sub}}-\varepsilon_a}{\varepsilon_{\text{sub}}+\varepsilon_a}\vec{\vec{G}}_s(\vec{r},\vec{r}';\omega), \quad (26)$$

where $\vec{\vec{G}}'_s(\vec{r},\vec{r}';\omega)$ has the following elements:

$$G'_{s,xx}(\vec{r},\vec{r}';\omega)=\frac{2(x-x')^2-(y-y')^2-(z+z')^2}{R'}, \quad (27)$$

$$G'_{s,xy}(\vec{r},\vec{r}';\omega)=\frac{3(x-x')(y-y')}{R'}, \quad (28)$$

$$G'_{s,xz}(\vec{r},\vec{r}';\omega)=-\frac{3(x-x')(z+z')}{R'}, \quad (29)$$

$$G'_{s,yx}(\vec{r},\vec{r}';\omega)=G'^{s}_{xy}(\vec{r},\vec{r}';\omega), \quad (30)$$

$$G'_{s,yy}(\vec{r},\vec{r}';\omega)=\frac{2(y-y')^2-(x-x')^2-(z+z')^2}{R'}, \quad (31)$$

$$G'_{s,yz}(\vec{r},\vec{r}';\omega)=-\frac{3(y-y')(z+z')}{R'}, \quad (32)$$

$$G'_{s,zx}(\vec{r},\vec{r}';\omega)=-G'^{s}_{xz}(\vec{r},\vec{r}';\omega), \quad (33)$$

$$G'_{s,zy}(\vec{r},\vec{r}';\omega)=-G'^{s}_{yz}(\vec{r},\vec{r}';\omega), \quad (34)$$

$$G'_{s,zz}(\vec{r},\vec{r}';\omega)=-\frac{2(z+z')^2-(x-x')^2-(y-y')^2}{R'}, \quad (35)$$

with $R'=[(x-x')^2+(y-y')^2+(z+z')^2]^{5/2}$. In the case of objects deposited on surfaces, we must add to the surface Green's tensor the homogeneous one, $\vec{\vec{G}}^0(\vec{r},\vec{r}';\omega)$, as we have seen before because we are in the $z'>0$ and $z>0$ region of dielectric permittivity $\varepsilon_a(\omega)$.

III. DIELECTRIC OBJECTS

A $100\times100\times40$ nm^3 dielectric object is illuminated at $\lambda=633$ nm through a glass substrate under the condition of total internal reflection. The angle of incidence is 60°. The detection is performed at $e=100$ nm above the pad of dielectric permittivity $\varepsilon=10.0$. We compute the total intensity associated to the electric field and to each Cartesian component for the TE mode (Fig. 2) and for the TM mode (Fig. 3). The intensities are normalized according to the incident light. It is known that in the near-field optics, a strong z component of the electric field exists since this one does not appear in reflectivity/transmission or in the scattering computations for far-field. Moreover, it is also important to see its evolution with the incident polarization (TE and TM modes).

In the TE mode, we can see first that the intensity associated to the total electric field shows a confinement of the electric field close to the lateral sides of the pad along the x direction [Fig. 2(a)]. Nevertheless, interference phenomena due to the backward scattering effects of the incident light on the object are more accentuated in the near-field optical image [Fig. 2(a)]. Second, we can see that the x component of the electric field, which is the incident one, is major [Fig. 2(b)] compared to the others [y and z components in Figs.

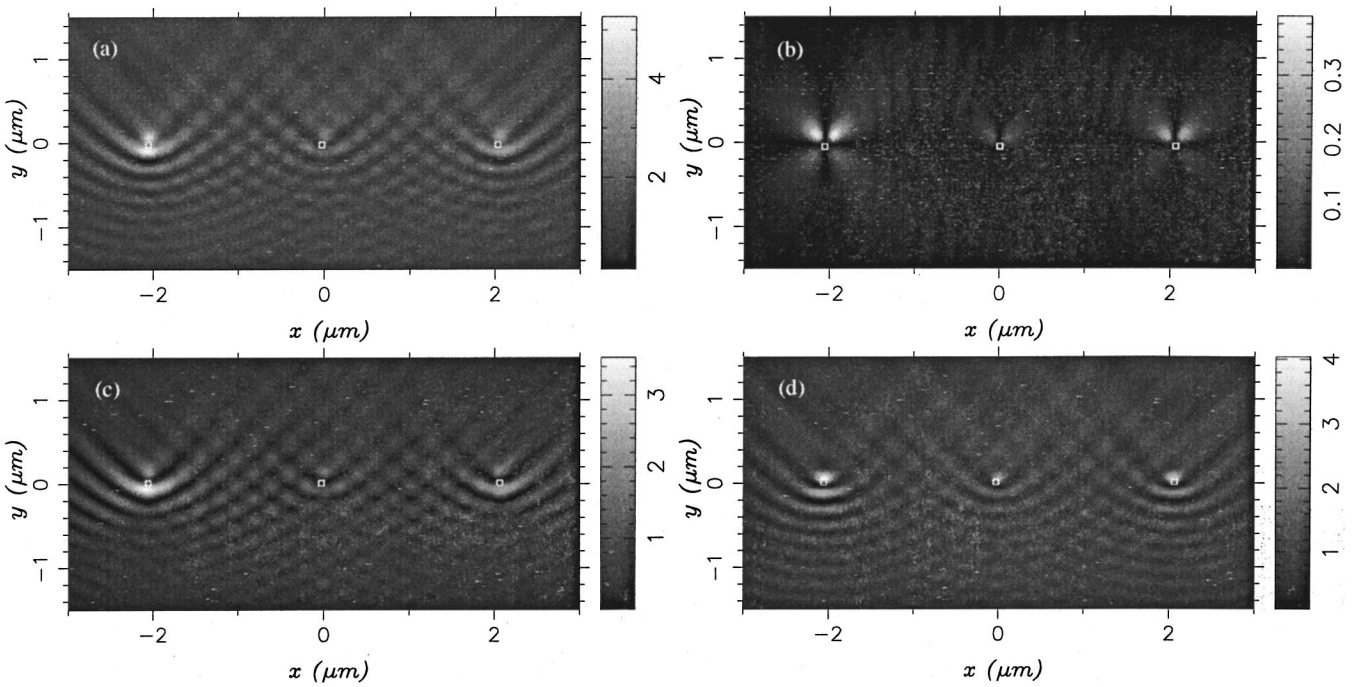

FIG. 7. An aluminum (left), a gold (middle), and a chromium pad of $100\times100\times40$ nm^3 are deposited on a glass substrate. The incident beam is TM polarized with $\lambda=400$ nm. (a) Variation of the intensity associated with the total electric field. (b) Variation of the intensity associated with the x component of the electric field. (c) Variation of the intensity associated with the y component of the electric field. (d) Variation of the intensity associated with the z component of the electric field. The detection is performed at $e=100$ nm above the metallic pad.

2(c) and 2(d)]. We can see in Fig. 2(c) that the interferences on the images due to the backscattering reflected wave on the object disappeared. Only the effects due to the confinement of the field around the object show up and are related to the topography of the object on the surface.

The same behavior can be seen in Fig. 2(d) for the z component of the electric field, which shows optical effects due to the topography of the object. However, the intensities are greater for this component [Fig. 2(d)] compared to the other one [Fig. 2(c)]. This shows the predominance of the z component of the electric field compared to the one parallel to the surface (y component) in the near-field optical images. We can see that the y component and the z-component represent, respectively, 0.5% and 2.5% of the intensity associated to the total electric field. Moreover, the y component shows an electric field which is well confined at the corners of the dielectric pad [Fig. 2(c)] whereas the z component displays the same strong effects on the lateral sides of the pad along the x direction [Fig. 2(d)]. By these optical patterns, we can distinguish the x component of the electric field from the z component.

In the TM mode, we can see first that the optical images for the intensity associated with the total electric field and for each Cartesian component are different compared to the TE mode. Consequently, the polarization plays an important role when analyzing the effects in the near-field optics. In this mode, we can see first that the intensity associated with the total electric field shows a confinement of the electric field above the upper side of the dielectric pad along the z direction [Fig. 3(a)]. As in the TE mode, interference phenomena on the surface due to the backward scattering effect of the incoming light on the dielectric object show up in the optical image [Fig. 3(a)]. Second, the y component and more particularly the z component of the electric field which are associated with the incident one are major [Figs. 3(c) and 3(d)] compared to the other one [x component in Fig. 3(b)]. We can see in Fig. 3(b) that the interferences on the images due to the backscattering reflected wave on the object disappeared. Only the effects due to the confinement of the field around the object show up and are related to the topography of the object on the surface as in the TE mode.

We can thus see that the x component, the y component, and the z component represent, respectively, 0.5%, 24.5%, and 75% of the total intensity. We also show in this case that the z component of the electric field is stronger in the near-field optical images compared to the y one. Moreover, the x component shows an electric field which is well confined on lateral sides (along the x direction) and also on the corners of the pad [Fig. 3(b)], whereas the y component and the z component display both interferences due to the incident light and a confinement of the electric field, respectively, on the lateral sides along the y direction and on the top of the pad along the z direction [Figs. 3(c) and 3(d)]. It is thus possible to distinguish these three components in the near-field optics. The forward scattering ($y>0$) shows up in the optical images [Fig. 2(a) and Fig. 3(a)].

Thanks to this study, we show that the analysis of polarization in the near-field optics leads to eliminating interferences on the surface. This analysis also shows the weight of each Cartesian component in the near-field optical images.

Similar effects can be found for any kind of material of real positive dielectric permittivity. The behaviors are accentuated as the dielectric permittivity increases. Nevertheless, the intensity variations associated to the component that was

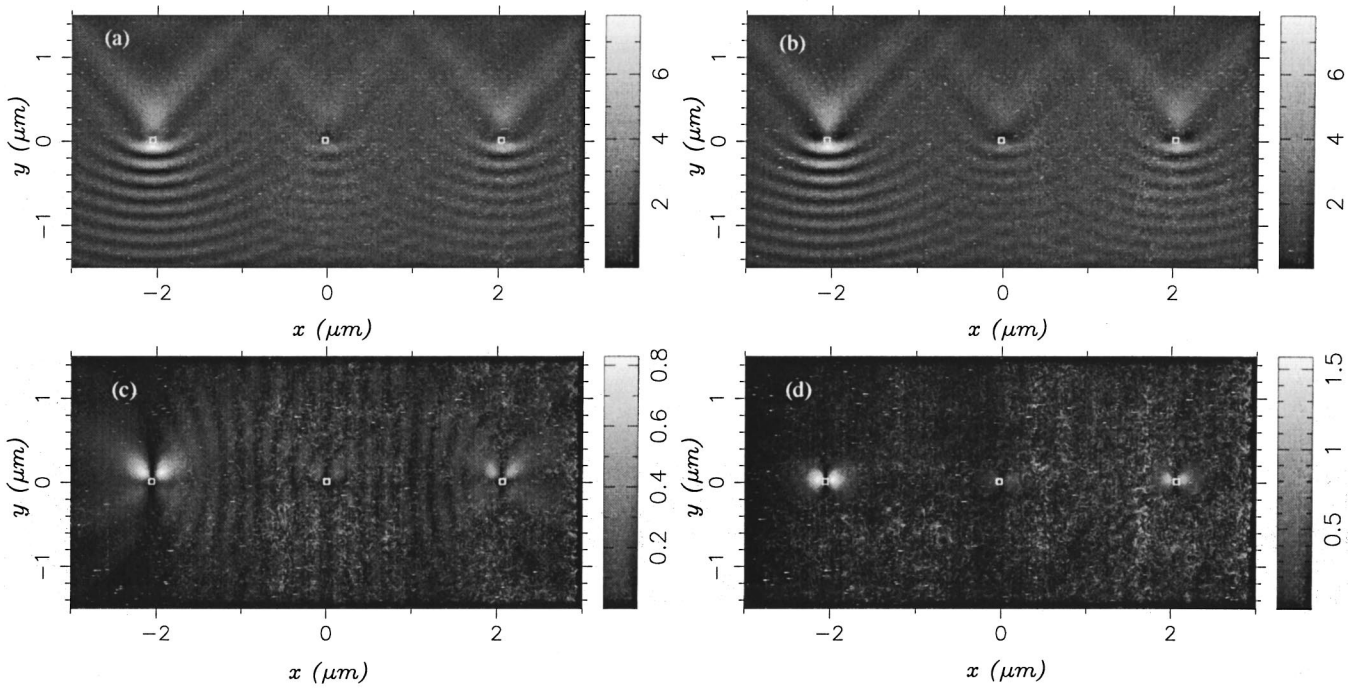

FIG. 8. An aluminum (left), a gold (middle), and a chromium pad of $100\times100\times40$ nm^3 are deposited on a glass substrate. The incident beam is TE polarized with $\lambda=400$ nm. (a) Variation of the intensity associated with the total electric field. (b) variation of the intensity associated with the x component of the electric field. (c) Variation of the intensity associated with the y component of the electric field. (d) Variation of the intensity associated with the z component of the electric field. The detection is performed at $e=100$ nm above the metallic pad.

not in the polarization of the incoming light (for the TE mode, y and z components; for the TM mode, x component) are not sufficiently high to detect them experimentally. In an experimental setup, it is necessary to have almost 10% of the total intensity to detect this polarization effect properly using the photon scanning tunneling microscope configuration. Metallic objects which show high increasing intensity effects associated to each Cartesian component in the near-field optics are thus more suitable.

Particularly, the localized plasmon resonance of noble metals leads to an enhancement of the electric field around nanoscopic objects in the near-field optical images. This field enhancement can also be detected in the far-field scattering cross-section spectra [18]. Moreover, we will use in Sec. IV different metallic materials in order to show the role of absorption behaviors in the optical images at the same constant height. Consequently, it is necessary to make spectroscopic computations by varying the incident wavelength. This technique shows which wavelength, in the visible range, demonstrates an exaltation of the electric field due to the metallic properties of the object in the near-field optics.

IV. METALLIC OBJECTS

In this section, we choose to study three different usual metallic materials, i.e., gold, aluminum, and chromium. Gold is used as a generic noble metal (as copper and silver) and shows a localized plasmon resonance behavior for nanometric objects. Aluminum is well-known for its high reflecting properties. As a comparison, we will finally study chromium, which has approximately the same absorption of aluminum but no such strong reflectivity in the visible range.

We illuminate a $100\times100\times40$ nm^3 Au pad through a glass substrate under the condition of total internal reflection with an angle of incidence of 60°. To check resonance behaviors, we compute the intensity associated to the total electric field and to the Cartesian components in order to see if the increase of the total intensity provides enhancement of the other components.

First, to check the reliability of the numerical technique, we calculate the maximum intensity associated to the total electric field for the Au pad as a function of the incident wavelength for the TE and TM modes [Fig. 4(a)]. This lateral size $d=100$ nm of the gold particle was chosen because it leads to the excitation of the localized plasmon resonance for a wavelength close to the HeNe one ($\lambda=640$ nm), which was shown in previous papers [10,18]. In Fig. 4(a), we can see an increase of the intensity, which is materialized by a peak in its variation with the incident wavelength at $\lambda=640$ nm for both TM and TE modes.

A localized plasmon resonance depends on the lateral sizes of the particle and also on the index of refraction of the surrounding medium. If we increase the lateral sizes, the peak corresponding to the localized plasmon excitation will be shifted to higher wavelengths [18]. The metallic object reacts as a dipole parallel to the surface [19] and emits light mainly perpendicularly to the dipole axis. Moreover, the angle of incidence does not change the emission wavelength in transmission for which the localized plasmon resonance takes place [18].

We show in Figs. 4(b) and 4(c) the variations of the intensities associated to each Cartesian component in both TE and TM modes. We can see that the resonance at λ

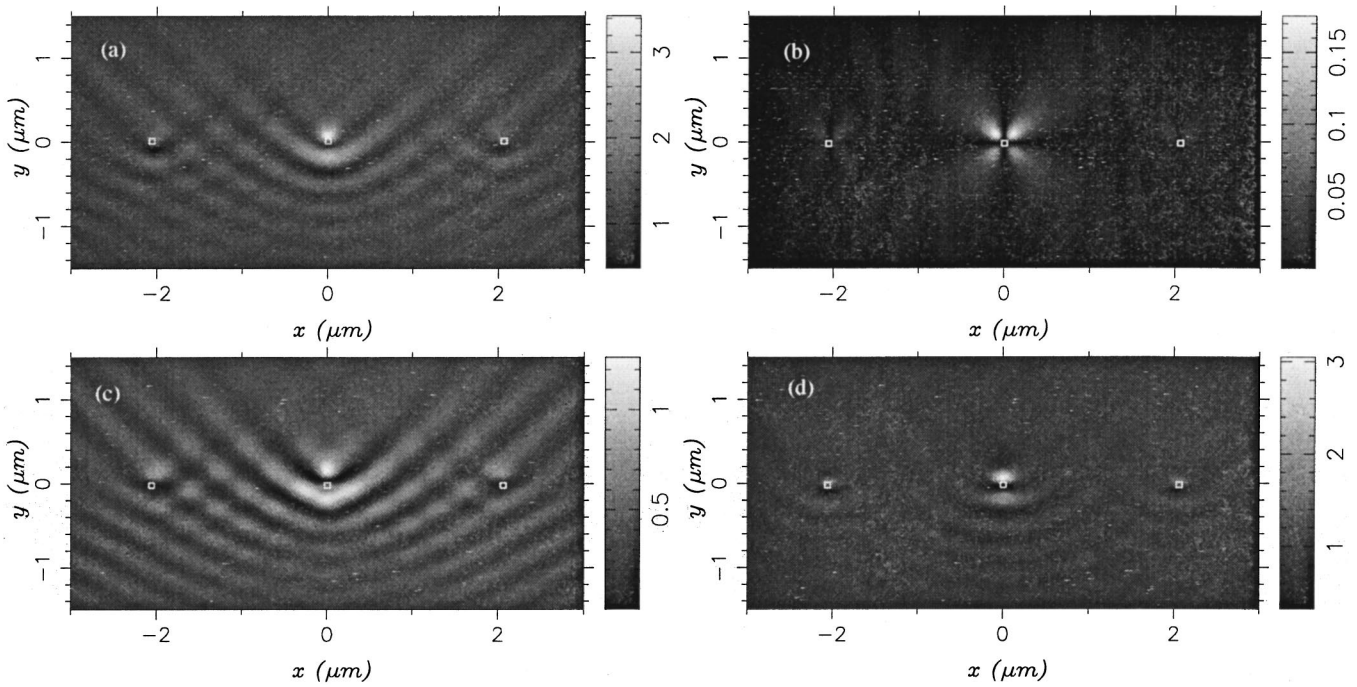

FIG. 9. An aluminum (left), a gold (middle), and a chromium pad of $100\times100\times40$ nm^3 are deposited on a glass substrate. The incident beam is TM polarized with $\lambda=633$ nm. (a) Variation of the intensity associated with the total electric field. (b) Variation of the intensity associated with the x component of the electric field. (c) Variation of the intensity associated with the y component of the electric field. (d) Variation of the intensity associated with the z component of the electric field. The detection is performed at $e=100$ nm above the metallic pad.

$=640$ nm increases the intensities of each component. As dielectric objects show, the z component is predominant compared to the y one created by the topography of the object for the TE mode in the near-field spectra [Fig. 4(c)]. The y component and the z component represent approximatively 10% and 35% of the intensity associated to the total electric field at 640 nm. Similarly, for the TM mode, the z component is major compared to the y one as for dielectric objects [Fig. 4(b)]. The x, y, and z components represent approximatively 10%, 30%, and 60% of the total intensity at 640 nm.

We can see also that there is an increase of the intensity associated to the total electric field and to its Cartesian components for wavelengths lower than 500 nm (Fig. 4). As a comparison, we did the same spectroscopy analysis for Al and Cr (Figs. 5 and 6). For $\lambda=633$ nm, we can see that the effects for the intensity variations are lower than those found at the localized plasmon resonance of Au but nevertheless higher than the dielectric case (Figs. 5 and 6). As for Au, the intensities associated to the total electric field and to each Cartesian component are greater for wavelengths lower than 500 nm for both modes of polarization TE and TM (Figs. 5 and 6). These effects can be attributed to the metallic aspect in the blue range and not to a localized plasmon resonance because this happens for the three different metals—gold, aluminum, and chromium—for the same wavelengths range lower than 500 nm (Figs. 4, 5, and 6).

For aluminum and chromium, this increase of the total intensity involves the enhancement for each Cartesian component [Figs. 5(b) and 5(c), 6(b) and 6(c)] as we saw for gold previously [Figs. 4(b) and 4(c)]. However, the effects are more accentuated for aluminum compared to chromium (Fig. 5 and Fig. 6) . These behaviors prove the role of absorption in the metallic materials. As chromium is a more absorbing one, the increased effects associated with the intensities are thus reduced for wavelengths lower than 500 nm compared to aluminum (Fig. 6).

We mapped the intensity associated with the total electric field and with each Cartesian component at constant height $e=100$ nm above three different pads: one in aluminum, one in gold, and another one in chromium. The maps were realized for two different wavelengths: $\lambda=400$ nm (Fig. 7 and Fig. 8) and $\lambda=633$ nm (Fig. 9 and Fig. 10). These were chosen to show the effects of aluminum and chromium at $\lambda=400$ nm and the localized plasmon resonance of gold for the HeNe wavelength. The optical images (Figs. 7 and 8) show that for $\lambda=400$ nm, the aluminum and the chromium pads show up in the intensity variations compared to the gold one. Moreover, the effects are accentuated for aluminum compared to chromium because Cr has more absorbing and less reflecting properties compared to Al. One could find the same effects for materials of similar reflecting properties with different absorption behaviors. This spectroscopy method leads to a new technique which enables us to recognize two similar materials in absorption but with different reflecting properties. We can see in Fig. 7(a) that the intensity associated with the total electric field is well confined on the upper side of the pads (along the z direction) for the TM mode and in Fig. 8(a) on the lateral sides of the pad in the TE mode (along the x direction).

Interference behaviors due to the backward scattering of the pads ($y<0$) show up in Fig. 7(a) and in Fig. 8(a). Moreover, the forward scattering ($y>0$) shows up in the optical images. If we analyze the intensity due to the x component of the electric field in the TM mode [Fig. 7(b)] and the intensity associated to the y component in the TE mode [Fig. 8(c)], we see that these scattering effects are eliminated and only con-

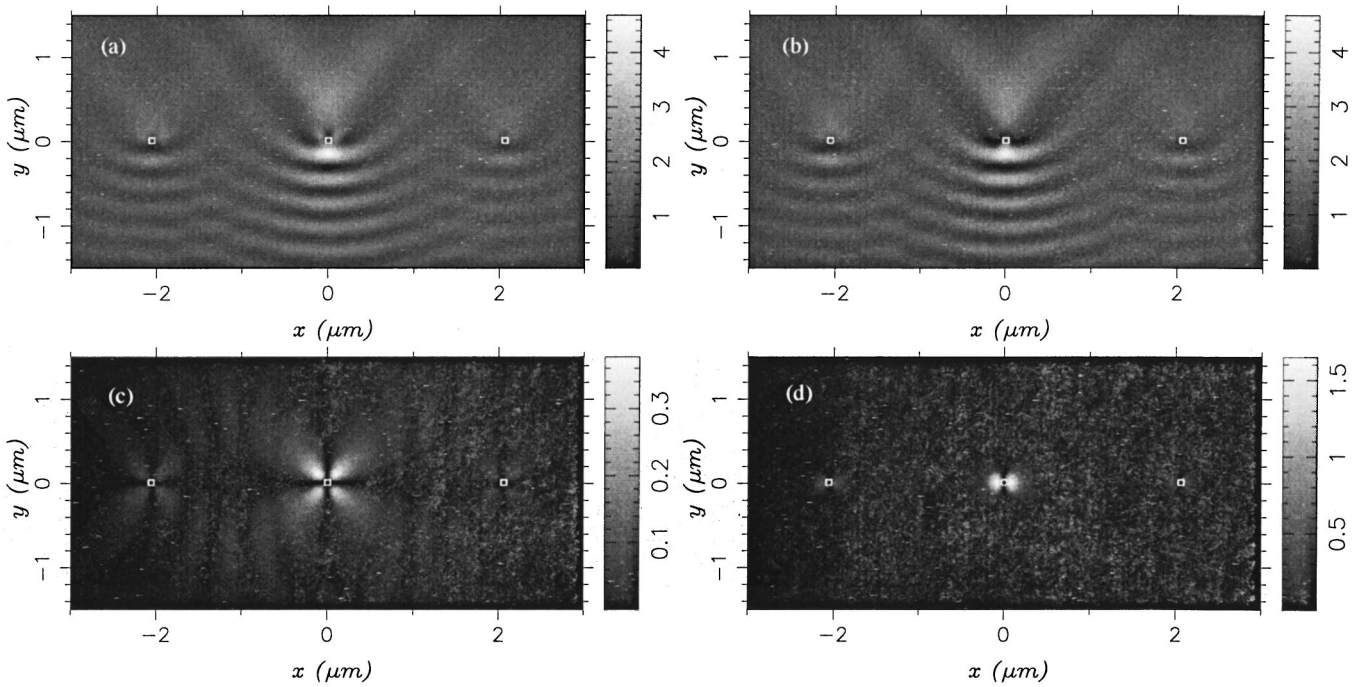

FIG. 10. An aluminum (left), a gold (middle), and a chromium pad of $100\times100\times40$ nm^3 are deposited on a glass substrate. The incident beam is TE polarized with $\lambda=633$ nm. (a) Variation of the intensity associated with the total electric field. (b) Variation of the intensity associated with the x component of the electric field. (c) Variation of the intensity associated with the y component of the electric field. (d) Variation of the intensity associated with the z component of the electric field. The detection is performed at $e=100$ nm above the metallic pad.

finement of the electric field on the corners of the pads due to the topography of the objects shows up in the optical images. As we saw for dielectric objects, the intensity associated with the z component of the electric field is major compared to the x and y ones in the TM mode and greater than the y one in the TE mode (Figs. 7 and 8). This z component of the electric field is well-confined on the upper side of the pad in the TM mode and on the lateral sides for the TE one as the dielectric objects show but with stronger effects due to the metallic properties [Fig. 7(d) and Fig. 8(d)].

Nevertheless, we can see that for the TE mode, the analysis of the optical image for the x component of the electric field shows different behaviors compared to dielectric objects: the confinement of the electric field along the x direction does not exist and the intensities are greater for metallic objects compared to dielectric ones. Similar effects can be analyzed for the gold pad at its localized plasmon resonance for the HeNe wavelength $\lambda=633$ nm (close to 640 nm) (Figs. 9 and 10). The effects for this wavelength are stronger for the gold particle compared to the Al and Cr ones because the localized plasmon resonance takes place and it involves an increase of the intensity associated with the total electric field and its Cartesian components.

V. CONCLUSION

The analysis of polarization in the near-field optics shows that it is possible to eliminate scattering behaviors associated with the total electric field by the detection of one of the Cartesian components for the electric field. The interferences are then completely eliminated. Only confinements due to the topography of the object are predominant in the near-field optical images by the analysis of the different components. Moreover, this study shows that a spectroscopic analysis performed by varying the incident wavelength is able to separate the resonance behaviors from the metallic properties (absorption) of the materials. The optical images realized for two different wavelengths show the possibility to distinguish Al, Cr, and Au particles at constant height. This procedure can be exploited experimentally in the PSTM configuration by the use of an analyzer placed at the exit of the fiber tip. Rotating the analyzer shows the possibility to detect at least one of the Cartesian components associated with the electric field. The extension to the SNOM configuration can be provided by a similar experimental technique. In this case, the analysis of polarization can be performed by placing an analyzer between the objective and the output detection and illuminating the system with fiber tip in near-field. This leads to an alternative method for the analysis of optical images in near-field optics.

ACKNOWLEDGMENTS

This work was financially supported by the European Community under Grant No. ERBFMRXCT980242. Professor O. Marti and the members of the ''Abteilung Experimentelle Physik'' are acknowledged. Special thanks are due to Stephanie Emonin for fruitful discussions.

[1] R. C. Reddick, R. J. Warmack, D. W. Chilcott, S. L. Sharp, and T. L. Ferrell, Rev. Sci. Instrum. **61**, 3669 (1990).
[2] R. C. Reddick, R. J. Warmack, and T. L. Ferrell, Phys. Rev. B **39**, 767 (1989).
[3] J. C. Weeber, E. Bourillot, A. Dereux, J. P. Goudonnet, Y. Chen, and C. Girard, Phys. Rev. Lett. **77**, 5332 (1996).
[4] D. W. Pohl, Adv. Opt. Electron. Microsc. **12**, 243 (1991).
[5] D. W. Pohl, U. C. Fischer, and U. T. Dürig, J. Microsc. **152**, 853 (1988).
[6] A. Dereux, E. Bourillot, J. C. Weeber, J. P. Goudonnet, Y. Chen, and C. Girard, Ann. Phys. Fr. **23**, 27 (1998).
[7] C. Girard, J. C. Weeber, A. Dereux, O. J. F. Martin, and J. P. Goudonnet, Phys. Rev. B **55**, 16 487 (1997).
[8] J. Zak, E. Moog, C. Liu, and S. Bader, J. Magn. Magn. Mater. **89**, 107 (1990).
[9] J. P. Jamet, S. Lemerle, P. Meyer, J. Ferre, B. Bartenlian, N. Bardou, C. Chappert, P. Veillet, F. Rousseaux, D. Decanini, and H. Launois, Phys. Rev. B **57**, 14 320 (1998).
[10] J. R. Krenn, A. Dereux, J. C. Weeber, E. Bourillot, Y. Lacroute, J. P. Goudonnet, G. Schider, W. Gotchy, A. Leitner, F. R. Aussenegg, and C. Girard, Phys. Rev. Lett. **82**, 2590 (1999).
[11] T. Klar, M. Perner, S. Grosse, G. Von Plessen, W. Spirkl, and J. Feldmann, Phys. Rev. Lett. **80**, 4249 (1998).
[12] M. Xiao, A. Zayats, and J. Siqueiros, Phys. Rev. B **55**, 1824 (1997).
[13] E. D. Palik, in *Handbook of Optical Constants of Solids*, edited by E. D. Palik (Academic Press, New York, 1991).
[14] A. A. Maradudin and D. L. Mills, Phys. Rev. B **11**, 1392 (1975).
[15] C. Girard and A. Dereux, Rep. Prog. Phys. **59**, 657 (1996).
[16] N. Richard, A. Dereux, T. David, E. Bourillot, J. P. Goudonnet, F. Scheurer, E. Beaurepaire, and G. Garreau, Phys. Rev. B **59**, 5936 (1999).
[17] A. Yaghjian, Proc. IEEE **68**, 248 (1980).
[18] O. Fallou, Ph.D. thesis, Université de Paris XI, Orsay, 1998.
[19] C. Bohren and D. Huffman, *Absorption and Scattering of Light by Small Particles* (John Wiley, New York, 1983).